RSC Advances

Check for updates

Chemical synthesis and super capacitance performance of novel CuO@Cu$_4$O$_3$/rGO/PANI nanocomposite electrode†

Abeer Enaiet Allah, [ID] *[ab] Fatma Mohamed,[abc] Mohamed A. Ghanem [ID] [d] and Ashour M. Ahmed [ID] [ce]

Copper oxide-based nanocomposites are promising electrode materials for high-performance supercapacitors due to their unique properties that aid electrolyte access and ion diffusion to the electrode surface. Herein, a facile and low-cost synthesis *in situ* strategy based on co-precipitation and incorporation processes of reduced graphene oxide (rGO), followed by *in situ* oxidative polymerization of aniline monomer has been reported. CuO@Cu$_4$O$_3$/rGO/PANI nanocomposite revealed the good distribution of CuO@Cu$_4$O$_3$ and rGO within the polymer matrix which allows improved electron transport and ion diffusion process. Galvanostatic charge–discharge (GCD) results displayed a higher specific capacitance value of 508 F g^{-1} for CuO@Cu$_4$O$_3$/rGO/PANI at 1.0 A g^{-1} in comparison to the pure CuO@Cu$_4$O$_3$ 278 F g^{-1}. CuO@Cu$_4$O$_3$/rGO/PANI displays an energy density of 23.95 W h kg^{-1} and power density of 374 W kg^{-1} at the current density of 1 A g^{-1} which is 1.8 times higher than that of CuO@Cu$_4$O$_3$ (13.125 W h kg^{-1}) at the same current density. The retention of the electrode was 93% of its initial capacitance up to 5000 cycles at a scan rate of 100 mV s^{-1}. The higher capacitance of the CuO@Cu$_4$O$_3$/rGO/PANI electrode was credited to the formation of a fibrous network structure and rapid ion diffusion paths through the nanocomposite matrix that resulted in enhanced surface-dependent electrochemical properties.

1 Introduction

Recently, there have been huge demands for renewable energy storage devices in daily life. Supercapacitors (SCs) are the main elements of energy storage worldwide because they possess a higher power density, significantly longer lifetimes, and rapid charge–discharge rate.[1–3] In general, SCs can be classified into electrical double-layer capacitors (EDLCs), pseudo-capacitors (PCs), and hybrid capacitors (HCs).[4,5] In EDLCs, the charge is stored electrostatically *via* reversible ion adsorption by forming an electric double layer at the porous carbon electrode–electrolyte interface. In contrast, the PCs store faradaic charges by

reversible redox chemical reactions that occur at the surface of the active materials such as conducting polymers (CPs), transition metal hydroxides (MHs), and oxides (MOs). By combining the EDLC and PC concepts, hybrid supercapacitors (HSCs) have emerged which can be prepared by a combination of a porous carbon electrode and metal oxide material. This combination of an electrode provides both high specific energy and high specific power as well as high cyclability and long cycle lifetime.[6,7]

Over the past decades, more efforts have been made to enhance the performance of the SCs which is fully dependent on the electrochemical properties of the electrode materials. The excellent electrode has a large specific surface area, high electrical conductivity, and good electrolyte wettability.[8,9] Electrode with a high surface area and high conductivity provides more electroactive sites and faster charge transfer for faradaic reactions as well as storing more double-layer charges.[10]

Cupric oxide (CuO) (tenorite) is a very attractive material for electrochemical applications due to its unique properties of good chemical stability, multiple oxidation states, desirable electrical conductivity, good theoretical specific capacitance, wide potential window, and fast faradaic redox reaction.[10,11] In addition, it is inexpensive, abundant, low toxicity, and easy to fabricate.[12] CuO is a well-established copper oxide material that has been extensively studied in the context of supercapacitors.

ᵃDepartment of Chemistry, Faculty of Science, Beni-Suef University, 62514 Beni-Suef City, Egypt

ᵇMaterials Science Lab, Chemistry Department, Faculty of Science, Beni-Suef University, Beni-Suef 62514, Egypt

ᶜNanophotonics and Applications Lab, Physics Department, Faculty of Science, Beni-Suef University, Beni-Suef 62514, Egypt

ᵈChemistry Department, College of Science, King Saud University, Riyadh 11451, Saudi Arabia. E-mail: mghanem@ksu.edu.sa

ᵉPhysics Department, College of Science, Imam Mohammad Ibn Saud Islamic University (IMSIU), Riyadh, 11623, Saudi Arabia. E-mail: ashour.elshemey@gmail.com

† Electronic supplementary information (ESI) available. See DOI: https://doi.org/10.1039/d4ra00065j
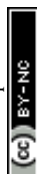
In contrast, Cu_4O_3 (paramelaconite) is a less explored copper oxide phase with unique properties. It is a rare black-colored material that crystallizes in the tetragonal crystal system.[13] It exhibits properties of a p-type semiconductor oxide, with a direct band gap of 2.34 eV and an indirect band gap of 1.50 eV, allowing it to absorb visible light effectively.[14] The unique aspect of Cu_4O_3 lies in its mixed-valence copper(I,II) oxide structure, as it contains both Cu^{1+} and Cu^{2+} oxidation states.[15] Positioned between cuprite (Cu_2O) and tenorite (CuO), it is classified as a binary copper oxide. Cu_4O_3 demonstrates a range of applications stemming from its distinctive structures, electronic configuration, and physicochemical properties.[16] Cu_4O_3 serves as a photocatalyst for diverse chemical reactions. Its antibacterial and cytotoxic properties make it valuable in medical applications. Furthermore, researchers have explored its potential in energy storage systems, such as Li-ion batteries, and its use as a material in magnetic spintronics. However, the synthesis of Cu_4O_3 faces significant challenges due to the difficulty in stabilizing both Cu(I) and Cu(II) states simultaneously.[17] This limitation hinders extensive research and practical applications, impeding the realization of its full potential. The electrode materials containing both CuO and Cu_4O_3 phases can enhance supercapacitor performance. This improvement can be attributed to the synergetic effects between the two phases. Integrating CuO with carbon nanomaterials has proved to be an efficient method for preparing excellent electrochemical devices.[18,19] Among different EDLCs carbon nanomaterials, reduced graphene oxide (rGO) has great potential for supercapacitor applications because of its excellent properties such as high cycling stability, high surface areas, high chemical stability, good electrical conductivity, strength, and tailoring.[20–23] On the other hand, graphene is often composed of a high number of graphitic stacks that are layered one on top of the other and have very little interlayer space in between. Consequently, graphene's capacitive performance as an electroactive material is limited since the electrical double-layer can only form on its outer surface.[24] Furthermore, the strong π–π interactions among neighboring sheets cause graphene sheets to re-stack and aggregate, reducing its high surface area and limiting the accessibility of electrolyte ions to the active sites of individual graphene sheets. These factors ultimately result in a major reduction in the capacitance of graphene sheets.

To improve the specific capacitance of graphene, its surface area must be accommodated with the abundant ions at the electrolyte/electrode interface, which causes the increment of the electrical double-layer capacitance. So, incorporating metal oxide nanoparticles as spacers between graphene sheets by fabricating graphene/metal oxide nanocomposites is a promising solution to address this issue.[25] Therefore, the combination of $CuO@Cu_4O_3$/rGO can form an electron-conducting network with a short charge diffusion path that enhances the charge transfer process and improves the supercapitance performance.[26,27]

Much previous literature has reported the supercapacitance performance of the CuO nanomaterial electrodes. For example, Shivaji et al. reported a specific capacitance of 57.44 F g^{-1} for CuO film in 1.0 M KOH electrolyte deposited by the electrodeposition protocol.[11] Kamatchi et al.[28] presented a CuO/rGO hybrid nanocomposite with a specific capacitance of 326 F g^{-1} at a current density of 0.5 A g^{-1}. In related studies, Miaomiao et al. showed that the capacitance for CuO/G was 213.05 F g^{-1} (ref. 29) while Ju et al.[30] synthesized CuO/Cu_2O/rGO nanocomposite by the hydrothermal method and the composite exhibits a specific capacitance of 470 F g^{-1} at a current density of 1.0 A g^{-1}. In addition, Xiangmao et al.[31] prepared rGO/Cu_2O/Cu as an electrode for a supercapacitor in 1.0 M KOH aqueous solution with a specific capacitance of 98.5 F g^{-1} at 1.0 A g^{-1} and Anand et al.[32] reported a specific capacitance of 493.75 F g^{-1} for CuO/PANI structure in 0.5 M H_2SO_4 solution. Unfortunately, these electrode materials suffer from relatively poor electrochemical efficiency due to their low electrical conductivity, high charge-transfer resistance, unstable cycling stability, and low cycling lifetimes.[33]

Today, incorporated inorganic materials in conductive polymers (CPs) matrix receive considerable attention to achieve better supercapacitive performance.[34] Polyaniline (PANI) is one of the most common conducting polymers due to its distinct superior chemical properties, good mechanical stability, appropriate electrical conductivity, and redox electroactivity process.[35] However, PANI during the charge/discharge process is mainly poor due to the degradation during long-term electrochemical cycle life as a result of low corrosion resistance. It is expected the incorporation of $CuO@Cu_4O_3$, rGO, and PANI materials in one nanocomposite can increase the supercapacitive activity through faradaic reactions, inhibit corrosion, and reduce interfacial resistance. The final properties of nanocomposites depend not only on the properties of the individual components, but also on the homogeneity of the dispersibility of the inorganics, and the interfacial between the interacted components.

Herein, we report a new attempt to incorporate copper oxide/reduced graphene oxide/polyaniline ($CuO@Cu_4O_3$/rGO/PANI) nanocomposite electrodes for supercapacitor application. To the best of our knowledge, the $CuO@Cu_4O_3$/rGO/PANI nanocomposite as a supercapacitor electrode achieved a significant capacitance measurement than other previously reported literature. The structural and physical properties are fully investigated using X-ray diffraction (XRD) analysis, Fourier-transform infrared (FTIR) spectroscopy, and scanning electron (SEM) microscopy. The electrochemical and supercapacitance properties of the $CuO@Cu_4O_3$/rGO/PANI samples were investigated through cyclic voltammetry, charge/discharge, and electrochemical impedance spectroscopy techniques.

2 Experimental work

2.1. Chemicals and materials

Potassium permanganate ($KMnO_4$), sodium nitrate ($NaNO_3$), copper(II) chloride dehydrate ($CuCl_2 \cdot 2H_2O$), and H_2O_2 were purchased from Al Nasr Company, Egypt. Hydrochloric acid (HCl), sulfuric acid (H_2SO_4), aniline monomer, and ammonium persulfate (APS, $H_8N_2O_8S_2$) were obtained from Sigma-Aldrich. Graphite powder was procured from Merck, Germany.

2.2. Preparation of CuO@Cu₄O₃

The preparation of CuO@Cu$_4$O$_3$ was executed by dissolving 10 g of copper(II) chloride dehydrate (CuCl$_2$·2H$_2$O) powder in 20 ml deionized water that was placed in a porcelain crucible and thermally decomposed at 550 °C in the air for 3 h to obtain CuO@Cu$_4$O$_3$. Then the CuO@Cu$_4$O$_3$ deposit was collected and minced in porcelain mortar and kept in a desiccator for further use.

2.3. Preparation of rGO

Firstly, the graphene oxide (GO) was prepared by adding about 2 g of graphite flakes into 200 ml of H$_2$SO$_4$ (98%) in a glass beaker. Subsequently, KMnO$_4$ and NaNO$_3$ were added and left to react for 5 h. Then, 500 mL of deionized water was added to the mixture, followed by the addition of H$_2$O$_2$ under stirring for 1 h. The obtained mixture was bright yellow, an indication of GO formation. The obtained GO solution was filtered and repeatedly washed with diluted HCl and deionized water until the pH of the solution became 7. Finally, the solution was centrifuged and dried for 12 h at 60 °C to obtain GO powder. GO was reduced into rGO using hydrazine hydrate following the literature.[36,37] The rGO was successively precipitated out and the obtained black powder was washed, filtered, and dried.

2.4. Preparation of CuO@Cu₄O₃/PANI and CuO@Cu₄O₃/rGO/PANI nanocomposites

In a typical synthesis, 1.0 ml of aniline monomer was dissolved in 4.0 ml of HCl and 100 ml of deionized water for 1.0 h. About 2.7 g of APS and 0.5 g of CuO@Cu$_4$O$_3$ were suspended in 100 ml of deionized water using sonication. The polymerization reaction is carried out by mixing the aniline and APS/CuO@Cu$_4$O$_3$ solutions at room temperature for 1.0 h. Finally, the resultant nanocomposite was filtered, washed, dried, and collected for studies. The CuO@Cu$_4$O$_3$/rGO/PANI nanocomposite was prepared following the above CuO@Cu$_4$O$_3$/PANI nanocomposite synthesis procedure but with the addition of 0.05 g of rGO. Finally, the resultant nanocomposite was filtered, washed, dried, and collected for studies.

2.5. Physicochemical characterizations of the CuO@Cu₄O₃/rGO/PANI nanocomposites

The prepared samples were analyzed using the X-ray diffractogram (XRD, Rigaku D/Max 2500), at 40 kV and 30 mA. The interlayer spacing (d-spacing) and crystal size (D) are calculated by using Bragg and Sherrer equations. Fourier transform infrared spectroscopy (FT-IR, NICOLET 6700) was used to check the functional group attached to the prepared materials. The morphology of the prepared samples were recorded using field emission scanning electron microscopy (FESEM, ZEISS, EVOMA10).

2.6. Electrodes preparation and electrochemical measurements

In a typical experiment, the substrate was made of graphite (G) paper with an area of (1.0 × 1.0 cm^2) was cleaned with ethanol,

then dried at 60 °C for 30 minutes. The nanocomposite ink was prepared by mixing 2.0 mg of each sample in 400 µL of 1 : 2 (v/v) isopropanol/water containing 20 µL of 5.0 wt% Nafion solution. Then the ink mixture was placed in the ultrasonic bath for 30 min to obtain homogenous suspension. The nanocomposite electrode was prepared by applying mass loading of 1 mg onto flexible graphite paper and allowed to dry at 60 °C using a hot air oven.

The electrochemical measurements were conducted using an electrochemical workstation (CHI660E) in a three-electrode mode using a 100 ml glass cell and under ambient conditions of 25 °C and 1.0 atmospheric pressure. The Ag/AgCl electrode was used as the reference electrode while the Pt mesh (1.0 × 1.0 cm^2) as a counter electrode in 1.0 M KOH as an aqueous electrolyte. The cyclic voltammetry and charge–discharge cycling tests were carried out at variable scan rates and different current densities. The electro-active materials were analyzed by electrochemical impedance spectroscopy in the frequency range between 0.1 Hz and 100 kHz.

The specific capacitance (C_g, F g^{-1}) was calculated using the following:

$$C = \frac{I \times t}{m \times \Delta V} \quad (1)$$

where I is the discharge current (A), t is the discharge time (s), m is the mass of active material (g), and ΔV is the potential change during the discharge process (V).

Energy density and power density can be calculated according to the following equation

$$E = \frac{1}{2}C_{cell}V^2 \quad (2)$$

$$P = \frac{E}{\Delta t} \quad (3)$$

3 Results and discussion characterization

3.1. Physicochemical characterizations of the CuO@Cu₄O₃/rGO/PANI nanocomposites

Fig. 1 displays the XRD patterns of the prepared pure CuO@Cu$_4$O$_3$, PANI, and CuO@Cu$_4$O$_3$/rGO/PANI nanocomposites. The XRD pattern of pure copper oxide (black line) fabricated by thermal oxidation of copper(II) chloride in the ambient atmosphere for 3.0 h at 550 °C. This XRD exhibited many sharp diffraction peaks indicating a polycrystalline structure with two main phases of CuO (tenorite) and Cu$_4$O$_3$ (paramelaconite). The phase of CuO has the highest intensity peaks, which means that it is the most dominant phase. Most of the XRD peaks belong to CuO phases (tenorite) with monoclinic structure and space group $C2/c$ based on card numbers JCPDS 00-045-0937 and JCPDS 00-001-1117.[38,39] Moreover, the XRD exhibited three main peaks at 2Θ of 33.62, 36.04, and 49.88° ascribed to the (110), (−111), and (−202) Bragg reflections, respectively. Many peaks of the CuO were detected at 2θ = 41.33, 58.03, 72.34, and 75.89° with Miller's index (002), (202), (311),
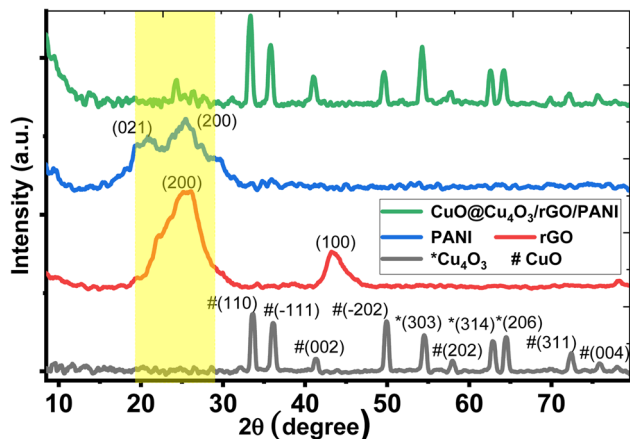
Fig. 1 The XRD patterns of as-prepared $CuO@Cu_4O_3$, rGO, PANI, and $CuO@Cu_4O_3/rGO/PANI$.

and (004), respectively. Besides, some peaks match to Cu_4O_3 phase located at $2\theta = 54.57$, 62.85, and 64.42° corresponding to diffraction planes (303), (314), and (206), respectively. The peaks of the Cu_4O_3 match with the tetragonal structure of pace group 141/amd following JCPDS card number 96-900-0604.

In the case of rGO, the XRD pattern (red line) shows an intense broad peak at 25.24° and a small peak at 43.16° which ascribed to (002) and (111) planes, respectively.[40] The (002) diffraction plane indicates the distance between rGO layers while the (111) diffraction plane indicates the short-ranger order of stacked G sheets.[41] The broadening of peaks means the stacking of rGO was not well ordered due to the lattice distortion of graphite that occurs during oxidation by $KMnO_4$.[42] Also, the broad peak may be attributed to very thin G layers due to the high degree of exfoliation and formation of a single or only a few layers of G sheets. The interlayer distance for the plane (002) was about 0.34 nm which showed the removal of oxygen moieties during the reduction process and good arrangement of the interlayer distance of G sheets.[36] The plane (001) is ascribed to the turbostratic band of disordered carbon materials[43] which confirms the formation of rGO sheets with considerably reduced oxygen content in the graphite precursor. The XRD pattern of PANI (blue line) revealed a semi-crystalline in nature with two characteristic diffraction peaks of PANI appeared at $2\theta = 20.35°$ (021) and $2\theta = 25.78°$ (200) corresponding to the perpendicular and parallel polymer chain periodicity respectively (JCPDS card no. 00-053-1891). The crystallinity may be ascribed to the duplication of quinoid and benzenoid rings in PANI chains.

For $CuO@Cu_4O_3/rGO/PANI$ nanocomposite (green line of Fig. 1) all peaks of $CuO@Cu_4O_3$ appeared in the XRD pattern with a change in intensity. In addition, a new small sharp diffraction peak was observed at 24.28° as an overlap between the peaks of G and PANI. This shows PANI and graphene's interaction and peaks were merged in the nanocomposite. The average crystal size for the main peaks (110), (−111), and (−202) of $CuO@Cu_4O_3$ increased from 541.86 A to 595.54 Å after the formation of $CuO@Cu_4O_3/rGO/PANI$ nanocomposite, respectively. This indicates enhancing the crystallinity of

nanocomposite that plays an important role in nanomaterials' physical and chemical properties.

FTIR spectra of the prepared materials recorded within the range of 400 to 4000 cm^{-1} at room temperature are presented in Fig. 2. The wide absorption band of $CuO@Cu_4O_3$ (black line) located at 3400 cm^{-1} attributed to the hydroxyl functional group (OH) as a result of adsorbed water molecules from the air. The two infrared absorption peaks at 559 and 465 cm^{-1} are due to the symmetric and asymmetric stretching of Cu–O vibrational modes which are in good agreement with the previous works.[43,44] The IR peak at 559 matches the diffraction plane (202), which indicates the formation of the monoclinic CuO phase.

FTIR spectrum of PANI (blue line) shows an absorption band around 3413 cm^{-1} matching with N–H stretching vibration mode of secondary amine. The absorption at 1478 is ascribed to C=N stretching vibrations in aromatic quinonoid units of PANI rings.[45] The presence of many bands in the range of 1100–1500 cm^{-1} reflects the oxidized form of PANI. In addition, two more bands appear at 1240 and 1119 cm^{-1} originating from the vibrational modes of symmetric C–N stretching and –NH– group of PANI.[46] However, the peak at 1295.86 cm^{-1} is ascribed to aromatic amine C–N stretching vibration in the benzene ring. The bands in the range 1200–500 cm^{-1} are due to the in-plane and out-of-plane bending of C–H in the aromatic ring. Moreover, the modes between 800–500 cm^{-1} are assigned to the *para* substitutions, *ortho* substitutions, and 1,3-disubstitution in the benzene ring, which agreed well with the PANI FTIR spectra reported in the literature.[47]

The FTIR spectrum in Fig. 2 shows many characteristic peaks of rGO (red line).[48,49] The O–H stretching vibrations appeared at 3389 cm^{-1} which means fully reduced graphene sheets due to deoxygenation. The broad bands between 2500 and 3200 cm^{-1} are from carboxyl COOH functional groups forming hydrogen bonds. The rGO exhibits a low-intensity peak around 1715 cm^{-1} indicating the presence of some C=O stretching of the carboxylic group. rGO possesses peaks located at 1549 and 1661 cm^{-1}
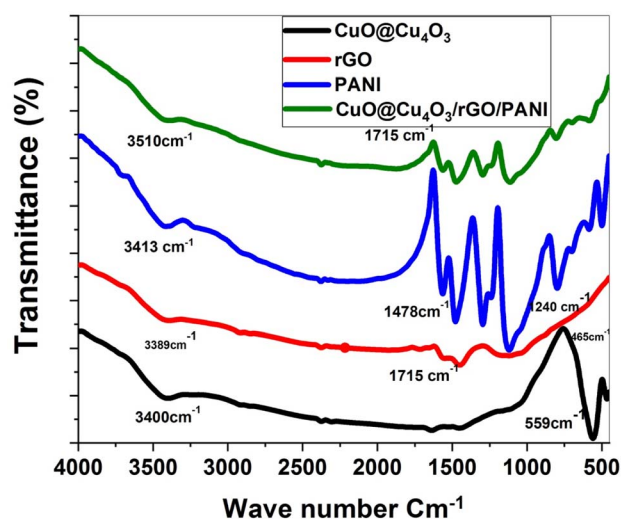

Fig. 2 FTIR spectra of the prepared $CuO@Cu_4O_3$, rGO, PANI, and $CuO@Cu_4O_3/rGO/PANI$.

attributed to C=C and C=C stretching in the graphene structure. The bands at 1150 and 1120 cm^{-1} showed C–O stretching of the epoxide and C–N stretching of the amine which indicates the formation of sp^2 honeycomb-like structure of rGO.

FTIR spectrum of the CuO@Cu$_4$O$_3$/rGO/PANI nanocomposite (purple line) shows the presence of Cu–O and N–H bond bands indicating the successful fabrication of CuO@Cu$_4$O$_3$/rGO/PANI nanocomposite. The shifting of some peaks is because of the incorporation of inorganic CuO@Cu$_4$O$_3$ into the polymer matrix while the disappearance of the C=O group at 1715 cm^{-1} indicates the complete reduction of GO to rGO.

Fig. 3 shows the scanning electron microscope (SEM) images of the surface morphology of CuO@Cu$_4$O$_3$, CuO@Cu$_4$O$_3$/PANI, and CuO@Cu$_4$O$_3$/rGO/PANI samples. The SEM image in Fig. 3(a) shows the surface of pure CuO@Cu$_4$O$_3$ has a star-shaped appearance made up of agglomerated nanorods surrounding a central point. Moreover, the surface of the star is covered by small cubic crystals and fragments of nanorods. On the other hand, the SEM of CuO@Cu$_4$O$_3$/PANI in Fig. 3(b) confirms the embedding of CuO@Cu$_4$O$_3$ within the PANI matrix with CuO@Cu$_4$O$_3$ maintaining its original shape of nanorod and cubic crystal morphology. While the PANI forms irregular micro-particles that appear to be composed of smaller particles agglomerated together.

Fig. 3(c) depicts the SEM image of the CuO@Cu$_4$O$_3$/rGO/PANI nanocomposite. It reveals the maintained morphology of the three components: CuO@Cu$_4$O$_3$, rGO, and PANI, within the overlapped matrix. Each part is clearly labeled in the illustration. Upon closer inspection of the high-magnification image (highlighted in yellow), it is observed that rGO displays a rippled and wrinkled sheet-like structure. This is consistent with its inherent flexibility and mechanical properties of rGO. The presence of these rGO layers separates the agglomerated matrix of PANI and the rods of CuO@Cu$_4$O$_3$, creating a free space that facilitates electron transfer and ion transport. The successful integration of CuO@Cu$_4$O$_3$, rGO, and PANI within the overlapped matrix plays a crucial role in generating synergistic effects, ultimately enhancing the overall electrochemical performance of the nanocomposite.

3.2. Electrochemical behavior and super capacitance performance of the CuO@Cu$_4$O$_3$/rGO/PANI nanocomposite

Owing to the unique properties of CuO@Cu$_4$O$_3$/rGO/PANI including high active sites, well-dispersed particles, and good
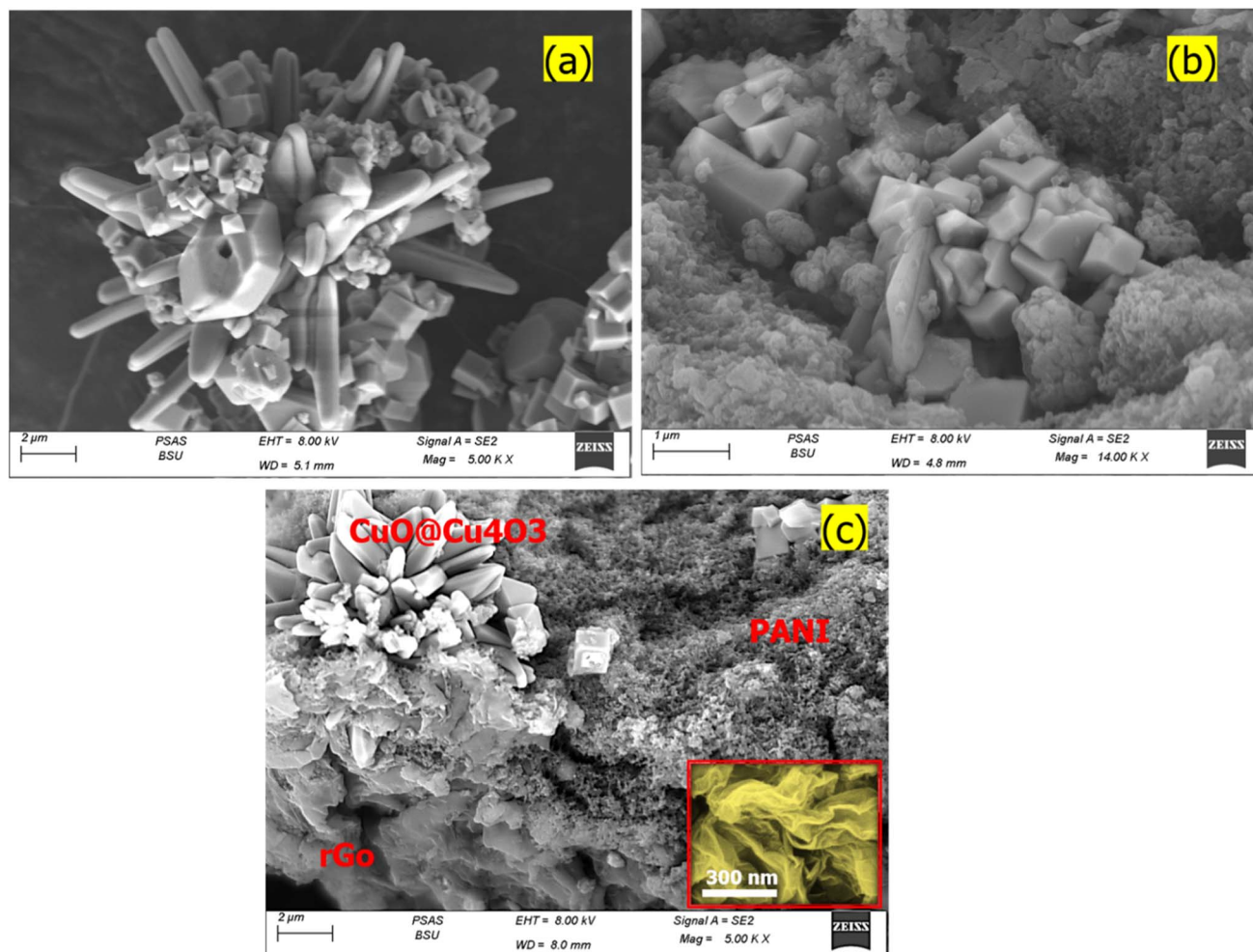
Fig. 3 SEM of the prepared samples (a) CuO@Cu$_4$O$_3$, (b) CuO@Cu$_4$O$_3$/PANI, and (c) CuO@Cu$_4$O$_3$/rGO/PANI nanocomposite.

conductivity, it is expected to be a promising candidate material for supercapacitor electrodes. To reveal the synergistic effect between CuO@Cu$_4$O$_3$, rGO, and PANI and to show the superiority of CuO@Cu$_4$O$_3$/rGO/PANI, the electrochemical performance was investigated in comparison to CuO@Cu$_4$O$_3$ and CuO@Cu$_4$O$_3$/PANI using a three-electrode system in 1.0 M KOH solution. Fig. 4(a) compares the cyclic voltammetry (CV) curves of pure CuO@Cu$_4$O$_3$, CuO@Cu$_4$O$_3$/PANI, and CuO@Cu$_4$O$_3$/rGO/PANI electrodes at a scan rate of 10 mV s^{-1}. Notably, a pair of redox peaks around 0.4/−0.7 V over the voltage range of −1 to 0.5 have appeared indicating a pseudocapacitive response of CuO@Cu$_4$O$_3$ (black line).[26] Additionally, the CV curves of CuO@Cu$_4$O$_3$/PANI displayed an extra three pairs of redox peaks that confirm the pseudocapacitive behavior of PANI. The peaks at −0.6/−0.7 are assumed to the redox transitions of PANI from leucoemeraldine to emeraldine, and peaks at −0.3/−0.45 represent the intermediates presence of hydroquinone/benzoquinone in a redox reaction, the peaks at 0.3/−0.25 represent the faradaic transformation from emeraldine to pernigraniline.[50,51] CuO@Cu$_4$O$_3$/rGO/PANI show a rectangular shape with considerable redox features, revealing the combined electrical double-layer charge storage effect of GO with the redox

behavior of CuO@Cu$_4$O$_3$ and PANI.[23] The CV curve of CuO@Cu$_4$O$_3$/rGO/PANI at 10 mV s^{-1} shows a much larger integrated area than that of CuO@Cu$_4$O$_3$ and CuO@Cu$_4$O$_3$/PANI, indicating that CuO@Cu$_4$O$_3$/rGO/PANI has a better capacitive property compared to CuO@Cu$_4$O$_3$ and CuO@Cu$_4$O$_3$/PANI. The enhanced capacitance behavior is assumed to increase the area of GO layers and the synergistic effect due to the combination of CuO@Cu$_4$O$_3$, rGO, and PANI. This effect can be assumed to be the redox reactions conferred by CuO@Cu$_4$O$_3$ and PANI in the electrode, leading to an increase in capacitance and a decrease in equivalent series resistance (ESR).[33]

Moreover, the rGO promotes the speed of charge transfer, high electrical conductivity, and enhanced electrical charge storage. At a high scan rate of 500 mV s^{-1}, the CV profile of CuO@Cu$_4$O$_3$/rGO/PANI still maintains the rectangular shape well, compared to CuO@Cu$_4$O$_3$ and CuO@Cu$_4$O$_3$/PANI (Fig. 4(b)). Moreover, the CV curves of CuO@Cu$_4$O$_3$/rGO/PANI at various scan rates from 10 to 500 mV s^{-1} showed a typical rectangular shape with a pair of redox peaks over the voltage range of −1 to 0.5, indicating significant rate capability.[52] Additionally, as the scan sweep increased the curve integrated area turned larger with a wider current density as shown in
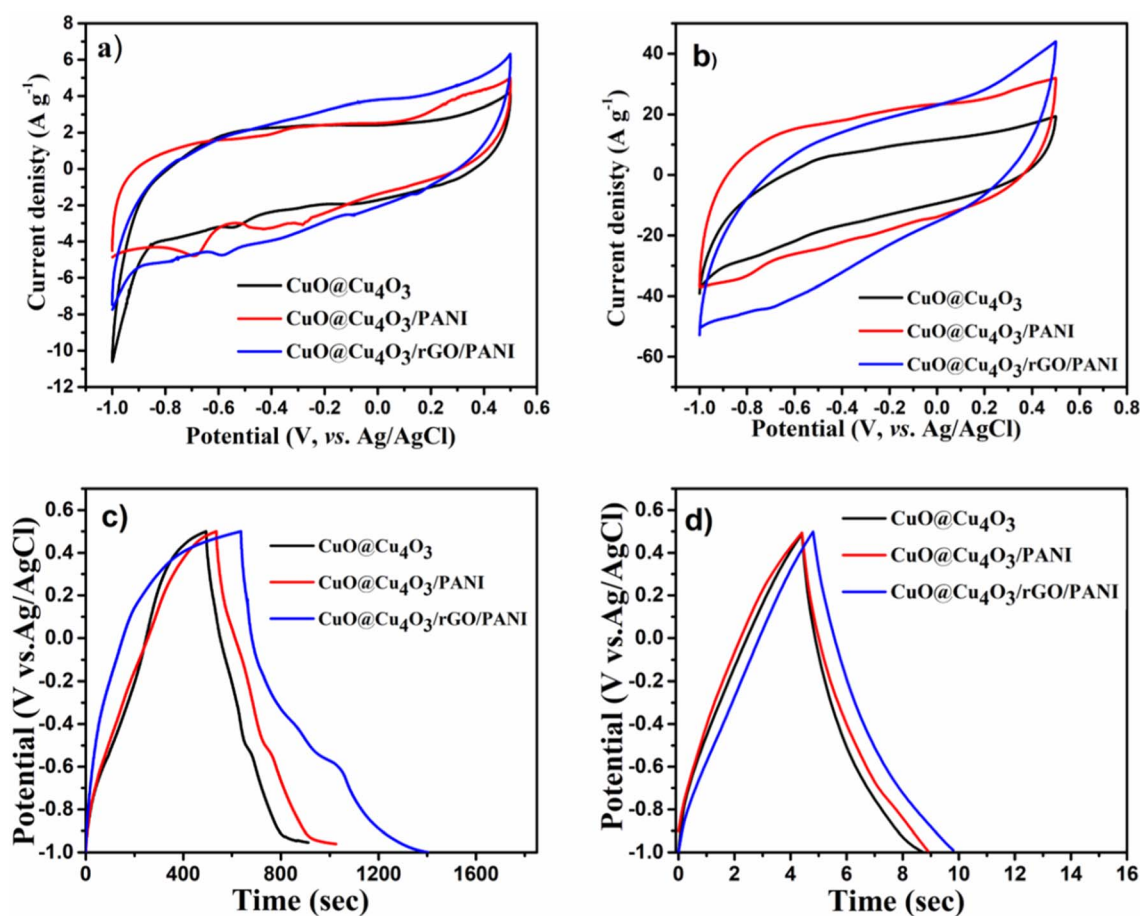

Fig. 4 (a) CV curves at 10 mV s^{-1} scan rate, (b) CV curves at 500 mV s^{-1} scan rate, (c) galvanostatic charge–discharge curves at a current density of 1 A g^{-1}, and (d) galvanostatic charge–discharge curves at a current density of 20 A for CuO@Cu$_4$O$_3$, CuO@Cu$_4$O$_3$/PANI, and CuO@Cu$_4$O$_3$/rGO/PANI.

Fig. S1.† These results imply its superior capacitive nature with superior ion response and outstanding rate capability.

The galvanostatic charge/discharge (GCD) curves of all electrodes at 1.0 A g^{-1} and 20 A g^{-1} are shown in Fig. 4(c) and (d), respectively. In addition, Fig. S2† shows the galvanostatic charge–discharge curves at different current densities for pure CuO@Cu$_4$O$_3$, CuO@Cu$_4$O$_3$/PANI, and CuO@Cu$_4$O$_3$/rGO/PANI nanocomposite electrodes. The results show a nearly isosceles triangle charge–discharge shape, at various applied current densities which further confirms the capacitive reversibility of all studied samples-based supercapacitors.

Fig. 5 displays the specific capacitance values of CuO@Cu$_4$O$_3$, CuO@Cu$_4$O$_3$/PANI, and CuO@Cu$_4$O$_3$/rGO/PANI electrodes as calculated based on the discharge curve and plotted against different current densities. The specific capacitance at 1.0 A g^{-1} of CuO@Cu$_4$O$_3$/rGO/PANI reaches 508 F g^{-1}, which is much higher than those of CuO@Cu$_4$O$_3$ (278 F g^{-1}) and CuO@Cu$_4$O$_3$/PANI (327 F g^{-1}) and other previously reported CuO hybrid electrodes that reported in Table 1. Moreover, as shown in Fig. 4(d), it achieves capacitance (133 F g^{-1}) at 20 A g^{-1} which is higher than CuO@Cu$_4$O$_3$ (119 F g^{-1}), and CuO@Cu$_4$O$_3$/PANI

(110 F g^{-1}). As expected, with increasing the current density to 20 A g^{-1}, the specific capacitance for CuO@Cu$_4$O$_3$/rGO/PANI exceeds those of other electrodes at all applied current densities. Further evidence for improvement of capacitive behavior that results from a combination of rGO with PANI and CuO@Cu$_4$O$_3$, measurements of single rGO and single PANI were conducted as shown in Fig. S3 and S4,† the calculated specific capacitance at 1.0 A g^{-1} for rGO and PANI are 71 and 66 F g^{-1}, respectively which are much lower than that of CuO@Cu$_4$O$_3$/rGO/PANI.

These results agree with a higher integrated area of the CV curve of CuO@Cu$_4$O$_3$/rGO/PANI reflecting its superior specific capacitance. Both the capacitance value and rate capability of CuO@Cu$_4$O$_3$/rGO/PANI far surpass those of CuO@Cu$_4$O$_3$ and CuO@Cu$_4$O$_3$/PANI which could be attributed to the synergy effect of the graphene EDLC and pseudo capacitance of polymeric PANI and copper oxide that offers the improved surface area and a continuous conducting network for electron transfer.[53]

To investigate the cycle stability, the CuO@Cu$_4$O$_3$/rGO/PANI nanocomposite electrode was exposed to 5000 cycles using CV

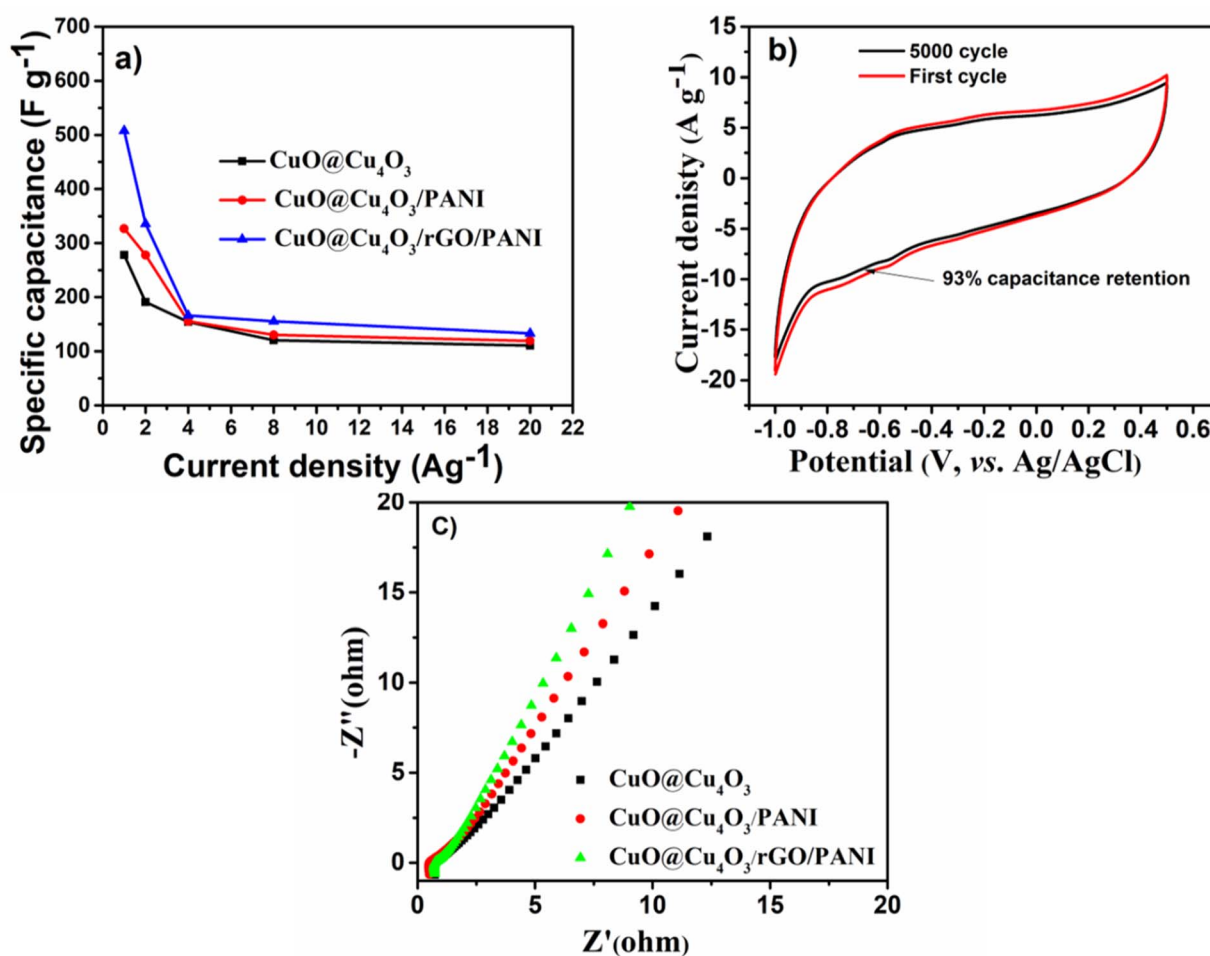Fig. 5 (a) specific capacitances at different current densities for CuO@Cu$_4$O$_3$, CuO@Cu$_4$O$_3$/PANI, and CuO@Cu$_4$O$_3$/rGO/PANI, (b) cycling performance of CuO@Cu$_4$O$_3$/rGO/PANI at 100 mV s^{-1}, and (c) Nyquist plots for CuO@Cu$_4$O$_3$, CuO@Cu$_4$O$_3$/PANI, and CuO@Cu$_4$O$_3$/rGO/PANI measured within the frequency range of from 100 kHz to 10 mHz.

Table 1 Comparison of the previously reported CuO/polymer composites with our CuO@Cu$_4$O$_3$/rGO/PANI electrode

Sample name	Electrolyte	Specific capacitance	Ref.
CuO/MnO$_2$	1 M Na$_2$SO$_4$	228 F g^{-1} at 0.25 A	57
CuO@MnO$_2$	1 M Na$_2$SO$_4$	343.9 F g^{-1} at 0.25 A g^{-1}	58
MnO$_2$/CuO	1 M KOH	161.5 F g^{-1} at 1 A g^{-1}	59
CuO/CNS	1 M Na$_2$SO$_4$	183.9 F g^{-1} at 0.1 A g^{-1}	33
	1 M KOH	371.1 F g^{-1} at 1.0 A g^{-1}	
PANi/CuO	1 M KCl	294 F g^{-1} at 0.05 A g^{-1}	60
3DCuO/GO	1 M Na$_2$SO$_4$	211 F g^{-1} at 1.0 A g^{-1}	61
CuO$_x$-C	6 M KOH	163 F g^{-1} at 0.1 A g^{-1}	62
CuO@Cu$_4$O$_3$/rGO/PANI	1 M KOH	508 F g^{-1} at 1.0 A g^{-1}	This study

at a scan rate of 100 mV s^{-1} in 1.0 M KOH solution as shown in Fig. 5(b). The CuO@Cu$_4$O$_3$/rGO/PANI nanocomposite shows high cycle stability with up to 93% retained capacitance of its initial value. The high capacitance retention is assumed to be the presence of rGO layers which confer conducting paths for electron flow, and the incorporation of CuO@Cu$_4$O$_3$ nanorods within the conductive PANI matrix creates extra active sites during the CV test and increases electron mobility through CuO@Cu$_4$O$_3$/rGO/PANI skeleton.

To further understand the improved capacitance performance with facilitated ion and electron transfer kinetics within CuO@Cu$_4$O$_3$/rGO/PANI nanocomposite, the electrochemical impedance spectroscopy (EIS) analysis was conducted for all electrodes in comparison and the results are shown in Fig. 5(c). All studied electrodes displayed a semi-depressed circle at a higher frequency rate, followed by one line at the lower frequency end. Clearly, the CuO@Cu$_4$O$_3$/rGO/PANI electrode shows much steeper linear gradients in the low-frequency sloped region than the pristine CuO@Cu$_4$O$_3$ and CuO@Cu$_4$O$_3$/PANI electrode (Fig. 5(c)), implying a faster ion diffusion than other samples. The intersection of the curves on the Z′ axis indicates the total resistance of the electrode/electrolyte system which combines the intrinsic resistance of active material, the contact resistance between the active material and the current collector, and the electrolyte resistivity system.[8]

To further evaluate the performance of CuO@Cu$_4$O$_3$/rGO/PANI as an electrode material for supercapacitors, the electrochemical analysis was also conducted using a symmetric cell. Fig. S5† presents the CV curves of the symmetrical supercapacitor at different scan rates in the potential windows of −1–0.5 V. The CV curves of CuO@Cu$_4$O$_3$/rGO/PANI maintain an optimal rectangular shape even at a high scan rate of 500 mV s^{-1}, pointing to the high-rate performance and good capacitive behavior.[54] The charge–discharge curves in Fig. S6† for CuO@Cu$_4$O$_3$, CuO@Cu$_4$O$_3$/PANI, and CuO@Cu$_4$O$_3$/rGO/PANI display quasi-triangular shape due to the contribution of the pseudocapacitive and EDLC behavior of the electrode materials owing to the presence of rGO, PANI, and CuO@Cu$_4$O$_3$. It is observed that increasing current density causes decreasing of charging/discharging time. This behavior is attributed to the requirement of less time for the attainment of the same potential difference across the two electrodes at a higher current density value.[55] Obviously, the CuO@Cu$_4$O$_3$/rGO/PANI achieved the highest specific capacitance of 155 F g^{-1} as

compared to 88 F g^{-1} for CuO@Cu$_4$O$_3$, and 100 F g^{-1} for CuO@Cu$_4$O$_3$/PANI at 1 A g^{-1}. The increment of specific capacitance from 88 F g^{-1} in CuO@Cu$_4$O$_3$ to 153 F g^{-1} in CuO@Cu$_4$O$_3$/rGO/PANI which is almost 1.7 times could be credited to the synergy of electric double-layer capacitance and pseudo capacitance. As previously indicated for CuO@Cu$_4$O$_3$/rGO/PANI, the large exposed surface area of CuO@Cu$_4$O$_3$ in open flowers structure, with redox active site contributed to pseudo capacitance so, the charge/discharge kinetics is qualitatively evaluated according to the following equation:

$$i = av^b \tag{4}$$

$$\log(i) = \log(a) + b\log(v) \tag{5}$$

where i and v are the current density and scan rate, while a and b are constants, respectively. Generally, the charge storage process depends on the value of the exponential index b. $b = 1$ or close to 1 this means electrochemical behavior is a surface-confined process dominated by electric double-layer capacitance, with fast reaction kinetics. When b is close to 0.5, the mechanism is a diffusion-controlled reaction and the dominant electrochemical behavior is pseudo capacitance with slow reaction kinetics. Fig. 6(a) presents the relationship of $\log(i)$ and $\log(v)$. The calculated b value for CuO@Cu$_4$O$_3$, CuO@Cu$_4$O$_3$/PANI, CuO@Cu$_4$O$_3$/rGO/PANI ranged from 0.47 to 0.60 in the charging process and ranged from 0.60 to 0.63 in discharging process which confirm the electrochemical behavior is dominant by pseudo capacitance.[55,56]

Trasatti method was used to calculate the percentage of contribution of both capacitances electric double-layer capacitance (C_{EDL}) and pseudo capacitance (C_{PC}) towards the total specific capacitance.[55] It includes the plotting of the inverse of specific capacitance ($1/C$) against the square root of scan rate (Fig. 6(b)). According to eqn (6) the Y-intercept of the linearly fitted line in the low scan rate region (Fig. S7†) provided the inverse of the total specific capacitance (C_T) of the electrode materials. Moreover for calculating the C_{EDL}, the specific capacitance (C) is plotted against the inverse of the square root of the scan rate Fig. 5(c). The value of y-intercept obtained by plotting the fitted line in a high scan rate region (Fig. S8†) represents C_{EDL} according to the next equations
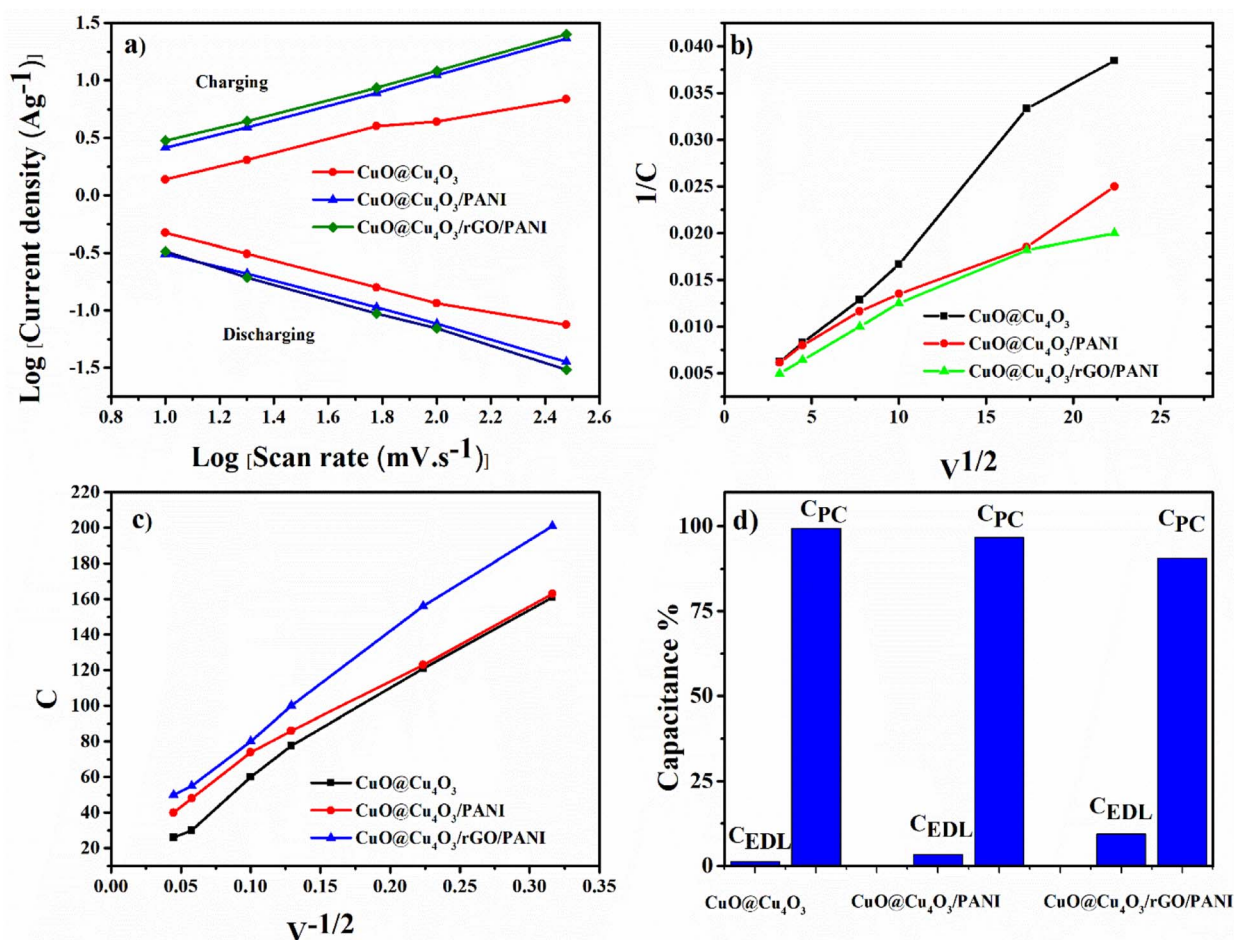
$$\frac{1}{C} = k_1\sqrt{v} + \frac{1}{C_T} \tag{6}$$

Fig. 6 (a) Linear plot of log *i* vs. log *ν* in both charge and discharge processes, (b) plot of 1/*C* versus √*v*, (c) plot of *c* versus/√*v*, (d) contribution of electric double-layer capacitance and pseudo capacitance for CuO@Cu₄O₃, CuO@Cu₄O₃/PANI and CuO@Cu₄O₃/rGO/PANI.

$$C = k_2 \frac{1}{\sqrt{v}} + C_{EDL} \tag{7}$$

The pseudo capacitance (C_{PC}) contribution was calculated by subtracting C_{EDL} from C_T. where k_1 and k_2 are the arbitrary constants. The percentage contribution of C_{EDL} and C_{PC} for CuO@Cu₄O₃, CuO@Cu₄O₃/PANI and CuO@Cu₄O₃/rGO/PANI was shown in Fig. 6(d). It is observed that CuO@Cu₄O₃ has 99% C_{PC} and 1% C_{EDL}, while CuO@Cu₄O₃/PANI has 96.5% C_{PC} and 3.5% C_{EDL}. Furthermore, on insertion of rGO into the matrix of CuO@Cu₄O₃/PANI led to the increments of C_{EDL} contribution to 10% due to the characteristic EDLC behavior of rGO as carbonic material.

To evaluate the utility of the prepared electrodes in the practical application of devices, the power density (P_s) and energy density (E_s) of electrode materials were computed and the comparison of Ragone plots for CuO@Cu₄O₃, CuO@Cu₄O₃/PANI and CuO@Cu₄O₃/rGO/PANI was presented in Fig. 7. The plot evinces that CuO@Cu₄O₃/rGO/PANI achieved the highest energy density as compared to other prepared electrode materials. CuO@Cu₄O₃/rGO/PANI displays an energy density of 23.95 W h kg⁻¹ and power density of 374 W kg⁻¹ at the current

density of 1 A g⁻¹ which is 1.8 times higher than that of CuO@Cu₄O₃ (13.125 W h kg⁻¹) at the same current density. These results reflect the synergistic effect of the combination of

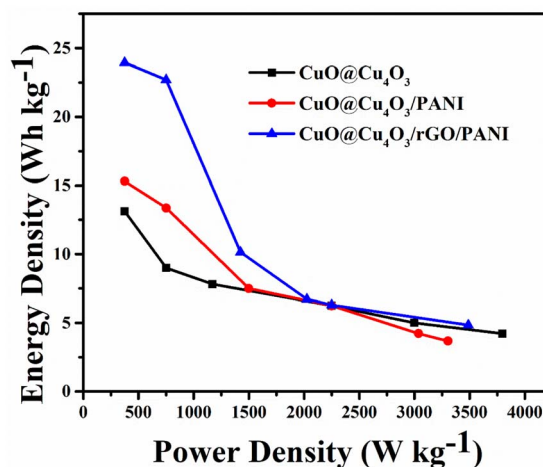Fig. 7 Ragone plot for CuO@Cu₄O₃, CuO@Cu₄O₃/PANI, and CuO@Cu₄O₃/rGO/PANI.

rGO into the polymeric matrix of CuO@Cu$_4$O$_3$/PANI. Furthermore, it is outstanding in comparison with previous literature[55]

4 Conclusion

A low-cost and easily fabricated catalyst for supercapacitors was prepared. It composed CuO@Cu$_4$O$_3$ and rGO with polyaniline in a homogeneous structure to form a CuO@Cu$_4$O$_3$/rGO/PANI composite. The well-characterized composite has a significant capacitance value than other previously prepared composites. It achieved a specific capacitance of 508 F g^{-1} at 1.0 A g^{-1} and attained capacitance retention of 93% after 5000 cycle. This was attributed to the synergy effect of the graphene EDLC and pseudo capacitance of polymer and copper oxide which offers improved surface area and a continuous network for electron transfer. Finally, the excellent energy storage capability shows that the CuO@Cu$_4$O$_3$/rGO/PANI composite could be a promising electrode material for supercapacitor applications.

Conflicts of interest

There are no conflicts to declare.

Acknowledgements

References

1 A. Gamal, M. Shaban, M. BinSabt, M. Moussa, A. M. Ahmed, M. Rabia, *et al.*, Facile Fabrication of Polyaniline/Pbs Nanocomposite for High-Performance Supercapacitor Application, *Nanomaterials*, 2022, **12**, 817, DOI: **10.3390/nano12050817**.

2 A. E. Allah, Y. Yamauchi, J. Wang, Y. Bando, H. Tan, A. A. Farghali, *et al.*, Soft-Templated Synthesis of Sheet-Like Nanoporous Nitrogen-Doped Carbons for Electrochemical Supercapacitors, *ChemElectroChem*, 2019, **6**(6), 1901–1907, DOI: **10.1002/CELC.201900151**.

3 Allah A. Enaiet, H. Tan, X. Xu, A. A. Farghali, M. H. Khedr, A. A. Alshehri, *et al.*, Controlled synthesis of mesoporous nitrogen-doped carbons with highly ordered two-dimensional hexagonal mesostructures and their chemical activation, *Nanoscale*, 2018, **10**, 12398–12406, DOI: **10.1039/C8NR02647E**.

4 A. E. Allah, J. Wang, Y. V. Kaneti, T. Li, A. A. Farghali, M. H. Khedr, *et al.*, Auto-programmed heteroarchitecturing: Self-assembling ordered mesoporous carbon between two-dimensional Ti3C2Tx MXene layers, *Nano Energy*, 2019, **65**, 103991, DOI: **10.1016/J.NANOEN.2019.103991**.

5 A. B. G. Trabelsi, D. Essam, H. Alkallas F., M. Ahmed A. and M. Rabia, Petal-like NiS-NiO/G-C3N4 Nanocomposite for High-Performance Symmetric Supercapacitor, *Micromachines*, 2022, **13**, 1–9, DOI: **10.3390/mi13122134**.

6 I. Shaheen, I. Hussain, T. Zahra, R. Memon, A. A. Alothman, M. Ouladsmane, *et al.*, ElectrophoreticFabrication of ZnO/CuO and ZnO/CuO/rGO Heterostructures-based Thin Films as Environmental Benign Flexible Electrode for Supercapacitor, *Chemosphere*, 2023, **322**, 138149, DOI: **10.1016/j.chemosphere.2023.138149**.

7 H. Kumar, R. Sharma, A. Yadav and R. Kumari, Recent advancement made in the field of reduced graphene oxide-based nanocomposites used in the energy storage devices: A review, *J. Energy Storage*, 2021, **33**, 102032, DOI: **10.1016/J.EST.2020.102032**.

8 A. E. Allah, Y. Yamauchi, J. Wang, Y. Bando, H. Tan, A. A. Farghali, *et al.*, Soft-Templated Synthesis of Sheet-Like Nanoporous Nitrogen-Doped Carbons for Electrochemical Supercapacitors, *ChemElectroChem*, 2019, 1–8, DOI: **10.1002/celc.201900151**.

9 G. Wang, L. Zhang and J. Zhang, A review of electrode materials for electrochemical supercapacitors, *Chem. Soc. Rev.*, 2012, **41**, 797–828, DOI: **10.1039/c1cs15060j**.

10 A. Abdisattar, M. Yeleuov, C. Daulbayev, K. Askaruly, A. Tolynbekov, A. Taurbekov, *et al.*, Recent advances and challenges of current collectors for supercapacitors, *Electrochem. Commun.*, 2022, **142**, 107373, DOI: **10.1016/J.ELECOM.2022.107373**.

11 S. B. Sadale, S. B. Patil, A. M. Teli, H. Masegi and K. Noda, Effect of deposition potential and annealing on performance of electrodeposited copper oxide thin films for supercapacitor application, *Solid State Sci.*, 2022, **123**, 106780, DOI: **10.1016/J.SOLIDSTATESCIENCES.2021.106780**.

12 A. Ghosh, M. Miah, A. Bera, S. K. Saha and B. Ghosh, Synthesis of freestanding 2D CuO nanosheets at room temperature through a simple surfactant free co-precipitation process and its application as electrode material in supercapacitors, *J. Alloys Compd.*, 2021, **862**, 158549, DOI: **10.1016/J.JALLCOM.2020.158549**.

13 G. M. Al-Senani, S. I. Al-Saeedi, N. S. Al-Kadhi, O. H. Abd-Elkader and N. M. Deraz, Green Synthesis and Pinning Behavior of Fe-Doped CuO/Cu2O/Cu4O3 Nanocomposites, *Process*, 2022, **10**, 729, DOI: **10.3390/PR10040729**.

14 C. M. A. Almazán, V. E. Santiago, R. López, H. S. López, H. C. V. Sánchez, A. Esparza, *et al.*, Cu4O3 thin films deposited by non-reactive rf-magnetron sputtering from a copper oxide target, *Rev. Mex. Fis.*, 2021, **67**, 495–499, DOI: **10.31349/RevMexFis.67.495**.

15 Y. Alajlani, F. Placido, A. Barlow, H. O. Chu, S. Song, R. S. Ur, *et al.*, Characterisation of Cu2O, Cu4O3, and CuO mixed phase thin films produced by microwave-activated reactive sputtering, *Vacuum*, 2017, **144**, 217–228, DOI: **10.1016/J.VACUUM.2017.08.005**.

16 J. Thanuja, N. G. Udayabhanu and H. R. Naika, Biosynthesis of Cu4O3 nanoparticles using Razma seeds: application to antibacterial and cytotoxicity activities, *SN Appl. Sci.*, 2019, **1**, 1–12, DOI: **10.1007/S42452-019-1556-3/FIGURES/11**.

17 A. Zivković, J. Sheehama, M. E. A. Warwick, D. R. Jones, C. Mitchel, D. Likius, *et al.*, Structural and electronic properties of Cu4O3 (paramelaconite): The role of native

impurities, *Pure Appl. Chem.*, 2021, **93**, 1229–1244, DOI: **10.1515/PAC-2021-0114/MACHINEREADABLECITATION/RIS**.

18 D. Khalafallah, J. Miao, M. Zhi and Z. Hong, Structuring graphene quantum dots anchored CuO for high-performance hybrid supercapacitors, *J. Taiwan Inst. Chem. Eng.*, 2021, **122**, 168–175, DOI: **10.1016/J.JTICE.2021.04.037**.

19 W. Xu, S. Dai, G. Liu, Y. Xi, C. Hu and X. Wang, CuO Nanoflowers growing on Carbon Fiber Fabric for Flexible High-Performance Supercapacitors, *Electrochim. Acta*, 2016, **203**, 1–8, DOI: **10.1016/J.ELECTACTA.2016.03.170**.

20 Y. M. Y. Albarqouni, P. L. Soon, A. M. A. Gomaa, A. S. Ethiraj, *et al.*, Facile synthesis of reduced graphene oxide aerogel in soft drink as supercapacitor electrode, *J. Nanostruct. Chem.*, 2022, **12**, 417–427, DOI: **10.1007/s40097-021-00424-7**.

21 S. Ishaq, M. Moussa, F. Kanwal, M. Ehsan, M. Saleem, T. N. Van, *et al.*, Facile synthesis of ternary graphene nanocomposites with doped metal oxide and conductive polymers as electrode materials for high performance supercapacitors, *Sci. Rep.*, 2019, **(9)**, 1–11, DOI: **10.1038/s41598-019-41939-y**.

22 A. Azhar, Y. Yamauchi, A. E. Allah, Z. A. Alothman, A. Y. Badjah, M. Naushad, *et al.*, Nanoporous iron oxide/carbon composites through in-situ deposition of prussian blue nanoparticles on graphene oxide nanosheets and subsequent thermal treatment for supercapacitor applications, *Nanomaterials*, 2019, **9**, 776, DOI: **10.3390/nano9050776**.

23 A. R. Ansari, S. A. Ansari, N. Parveen, M. O. Ansari and Z. Osman, Silver Nanoparticles Embedded on Reduced Graphene Oxide@Copper Oxide Nanocomposite for High Performance Supercapacitor Applications, *Mater.*, 2021, **14**(17), 5032, DOI: **10.3390/MA14175032**.

24 A. González, E. Goikolea, J. A. Barrena and R. Mysyk, Review on supercapacitors: Technologies and materials, *Renewable Sustainable Energy Rev.*, 2016, **58**, 1189–1206, DOI: **10.1016/j.rser.2015.12.249**.

25 S. Raj, S. K. Srivastava, P. Kar and P. Roy, In situ growth of Co3O4 nanoflakes on reduced graphene oxide-wrapped Ni-foam as high performance asymmetric supercapacitor, *Electrochim. Acta*, 2019, **302**, 327–337, DOI: **10.1016/j.electacta.2019.02.010**.

26 V. H. Luan, J. Hun, H. Wook and W. Lee, Highly porous and capacitive copper oxide nanowire/graphene hybrid carbon nanostructure for high-performance supercapacitor electrodes, *Composites, Part B*, 2019, **178**, 107464, DOI: **10.1016/j.compositesb.2019.107464**.

27 E. Sohouli, H. Teymourinia, A. Ramazani and K. Adib, Preparation of high-performance supercapacitor electrode with nanocomposite of CuO/NCNO flower-like, *Sci. Rep.*, 2023, **13**, 1–14, DOI: **10.1038/s41598-023-43430-1**.

28 K. K. Purushothaman, B. Saravanakumar, I. M. Babu, B. Sethuraman and G. Muralidharan, *RSC Adv.*, 2014, **4**, 23485–23491.

29 M. Zhai, A. Li and J. Hu, CuO nanorods grown vertically on graphene nanosheets as a battery-type material for high-performance supercapacitor electrodes, *RSC Adv.*, 2020, **10**, 36554–36561, DOI: **10.1039/D0RA06758J**.

30 X. Ju, X. Zhu, Z. Chang, L. Guo, C. Liao, Y. Zong, *et al.*, Controllable synthesis of porous CuO-Cu2O/rGO microspheres composite as high-performance electrode material for supercapacitors, *J. Alloys Compd.*, 2019, **27**, 845–858, DOI: **10.1080/09276440.2019.1707024**.

31 X. Dong, K. Wang, C. Zhao, X. Qian, S. Chen, Z. Li, *et al.*, Direct synthesis of RGO/Cu2O composite films on Cu foil for supercapacitors, *J. Alloys Compd.*, 2014, **586**, 745–753, DOI: **10.1016/J.JALLCOM.2013.10.078**.

32 S. Anand, Md W. Ahmad, A. K. A. Al Saidi, D.-J. Yang and A. Choudhury, *Mater. Chem. Phys.*, 2020, **254**, 123480.

33 X. Yuan, X. Yan, C. Zhou, J. Wang, D. Wang, H. Jiang, *et al.*, Decorating carbon nanosheets with copper oxide nanoparticles for boosting the electrochemical performance of symmetric coin cell supercapacitor with different electrolytes, *Ceram. Int.*, 2020, **46**, 435–443, DOI: **10.1016/j.ceramint.2019.08.280**.

34 S. Sardana, A. Gupta, K. Singh, A. S. Maan and A. Ohlan, Conducting polymer hydrogel based electrode materials for supercapacitor applications, *J. Energy Storage*, 2022, **45**, 103510, DOI: **10.1016/J.EST.2021.103510**.

35 N. M. A. Hadia, M. A. H. Khalafalla, S. F. M. Abdel, A. M. Ahmed, M. Shaban, A. H. Almuqrin, *et al.*, Conversion of Sewage Water into H2 Gas Fuel Using Hexagonal Nanosheets of the Polyaniline-Assisted Deposition of PbI2 as a Nanocomposite Photocathode with the Theoretical Qualitative Ab-Initio Calculation of the H2O Splitting, *Polymers*, 2022, **14**(11), 2148, DOI: **10.3390/polym14112148**.

36 G. Yasin, M. Arif, M. Shakeel, Y. Dun, Y. Zuo, W. Q. Khan, *et al.*, Exploring the Nickel–Graphene Nanocomposite Coatings for Superior Corrosion Resistance: Manipulating the Effect of Deposition Current Density on its Morphology, Mechanical Properties, and Erosion-Corrosion Performance, *Adv. Eng. Mater.*, 2018, **20**, 1701166, DOI: **10.1002/ADEM.201701166**.

37 F. T. Johra, J. W. Lee and W. G. Jung, Facile and safe graphene preparation on solution based platform, *J. Ind. Eng. Chem.*, 2014, **20**, 2883–2887, DOI: **10.1016/J.JIEC.2013.11.022**.

38 A. F. Zedan, N. K. Allam and S. Y. Alqaradawi, A Study of Low-Temperature CO Oxidation over Mesoporous CuO-TiO2 Nanotube Catalysts, *Catal*, 2017, **7**, 129, DOI: **10.3390/CATAL7050129**.

39 A. Bandyopadhyay, K. Mandal, V. Ambardekar, D. Das and S. B. Majumder, Electrophoretic deposition of CuO particulate thick film for ethanol sensing, *J. Mater. Sci.: Mater. Electron.*, 2021, **32**, 17324–17335, DOI: **10.1007/S10854-021-06247-0/FIGURES/10**.

40 A. Kumar, A. M. Sadanandhan and S. L. Jain, Silver doped reduced graphene oxide as a promising plasmonic photocatalyst for oxidative coupling of benzylamines under visible light irradiation, *New J. Chem.*, 2019, **43**, 9116–9122, DOI: **10.1039/C9NJ00852G**.

41 A. Pavithra, R. A. Rakkesh, D. Durgalakshmi and S. Balakumar, Room temperature detection of hydrogen gas using graphene based conductometric gas sensor, *J.*

Nanosci. Nanotechnol., 2017, **17**, 3449–3453, DOI: **10.1166/ JNN.2017.13054**.

42 K. Krishnamoorthy, M. Veerapandian, K. Yun and S. J. Kim, The chemical and structural analysis of graphene oxide with different degrees of oxidation, *Carbon*, 2013, **53**, 38–49, DOI: **10.1016/J.CARBON.2012.10.013**.

43 S. Joshi, R. Siddiqui, P. Sharma, R. Kumar, G. Verma and A. Saini, Green synthesis of peptide functionalized reduced graphene oxide (rGO) nano bioconjugate with enhanced antibacterial activity, *Sci. Rep.*, 2020, **10**, 1–11, DOI: **10.1038/s41598-020-66230-3**.

44 F. Buazar, S. Sweidi, M. Badri and F. Kroushawi, Biofabrication of highly pure copper oxide nanoparticles using wheat seed extract and their catalytic activity: A mechanistic approach, *Green Process. Synth.*, 2019, **8**, 691–702, DOI: **10.1515/GPS-2019-0040/ASSET/GRAPHIC/J_GPS-2019-0040_EQ_001.PNG**.

45 W. N. Benahmed, I. Bekri-Abbes and E. Srasra, Spectroscopic study of polyaniline/AgCl@Ag nanocomposites prepared by a one-step method, *J. Spectrosc.*, 2018, **2018**, 7320654, DOI: **10.1155/2018/7320654**.

46 G. Editors, J. Jaromír Klemeš, P. Yen Liew, W. Shin Ho, J. Shiun Lim, M. Rasyidi Husin, *et al.*, Fourier Transforms Infrared Spectroscopy and X-ray Diffraction Investigation of Recycled Polypropylene/Polyaniline Blends, *Chem. Eng. Trans.*, 2017, **56**, 1015–1020, DOI: **10.3303/CET1756170**.

47 B. Butoi, A. Groza, P. Dinca, A. Balan and V. Barna, Morphological and Structural Analysis of Polyaniline and Poly(o-anisidine) Layers Generated in a DC Glow Discharge Plasma by Using an Oblique Angle Electrode Deposition Configuration, *Polymers*, 2017, **9**(12), 732, DOI: **10.3390/POLYM9120732**.

48 C. Xu, X. Shi, A. Ji, L. Shi, C. Zhou and Y. Cui, Fabrication and Characteristics of Reduced Graphene Oxide Produced with Different Green Reductants, *PLoS One*, 2015, **10**, e0144842, DOI: **10.1371/journal.pone.0144842**.

49 R. Doufnoune, T. Baouz and S. Bouchareb, Influence of functionalized reduced graphene oxide and compatibilizer on mechanical, thermal and morphological properties of polypropylene/polybutene-1 (PP/PB-1) blends, *J. Adhes. Sci. Technol.*, 2019, **33**, 1729–1757, DOI: **10.1080/01694243.2019.1611367**.

50 M. F. Mousavi, M. Hashemi, M. S. Rahmanifar and A. Noori, Synergistic effect between redox additive electrolyte and PANI-rGO nanocomposite electrode for high energy and high power supercapacitor, *Electrochim. Acta*, 2017, **228**, 290–298, DOI: **10.1016/j.electacta.2017.01.027**.

51 S. B. Yoon, E. H. Yoon and K. B. Kim, Electrochemical properties of leucoemeraldine, emeraldine, and pernigraniline forms of polyaniline/multi-wall carbon nanotube nanocomposites for supercapacitor applications, *J. Power Sources*, 2011, **196**, 10791–10797, DOI: **10.1016/j.jpowsour.2011.08.107**.

52 R. Balu and A. Dakshanamoorthy, Synthesis of wool ball-like copper sulphide nanospheres embedded graphene nanocomposite as electrode for high-performance symmetric supercapacitor device, *Int. J. Energy Res.*, 2022, **46**, 6730–6744, DOI: **10.1002/er.7613**.

53 K. A. Lichchhavi and P. M. Shirage, A review on synergy of transition metal oxide nanostructured materials: Effective and coherent choice for supercapacitor electrodes, *J. Energy Storage*, 2022, **55**, 105692, DOI: **10.1016/J.EST.2022.105692**.

54 A. E. Allah, J. Wang, Y. V. Kaneti, T. Li, A. A. Farghali, M. H. Khedr, *et al.*, Auto-programmed heteroarchitecturing: Self-assembling ordered mesoporous carbon between two-dimensional Ti3C2Tx MXene layers, *Nano Energy*, 2019, **65**, 103991, DOI: **10.1016/j.nanoen.2019.103991**.

55 S. Ansari, R. B. Choudhary and A. Gupta, Nanoflower copper sulphide intercalated reduced graphene oxide integrated polypyrrole nano matrix as robust symmetric supercapacitor electrode material, *J. Energy Storage*, 2023, **59**, 106446, DOI: **10.1016/j.est.2022.106446**.

56 Y. J. Cao, C. Y. Lu, Z. W. Zhang, Z. Wang, Y. H. Kang, T. T. Yang, *et al.*, N/O Co-doped Porous Carbons Derived from Coal Tar Pitch for Ultra-high Specific Capacitance Supercapacitors, *ACS Omega*, 2022, **7**, 23342–23352, DOI: **10.1021/acsomega.2c01534**.

57 Z. Zhang, C. Ma, M. Huang, F. Li, S. Zhu, C. Hua, *et al.*, Birnessite MnO2-decorated hollow dandelion-like CuO architectures for supercapacitor electrodes, *J. Mater. Sci.: Mater. Electron.*, 2015, **26**, 4212–4220, DOI: **10.1007/S10854-015-2969-4**.

58 H. Chen, M. Zhou, T. Wang, F. Li and Y. X. Zhang, Construction of unique cupric oxide-manganese dioxide core-shell arrays on a copper grid for high-performance supercapacitors, *J. Mater. Chem. A*, 2016, **4**, 10786–10793, DOI: **10.1039/c6ta04258a**.

59 R. K. Mohamed, A. Manikandan, M. Mahendiran, P. Prabakaran, J. Madhavan and M. Victor Antony Raj, Fabrication of manganese oxide decorated copper oxide (MnO2/CuO) nanocomposite electrodes for energy storage supercapacitor devices, *Phys. E*, 2020, **119**, 114033, DOI: **10.1016/j.physe.2020.114033**.

60 S. P. Ashokkumar, H. Vijeth, L. Yesappa, M. Niranjana, M. Vandana and H. Devendrappa, Electrochemically synthesized polyaniline/copper oxide nano composites: To study optical band gap and electrochemical performance for energy storage devices, *Inorg. Chem. Commun.*, 2020, **115**, 107865, DOI: **10.1016/J.INOCHE.2020.107865**.

61 Z. Song, W. Liu, N. Sun, W. Wei, Z. Zhang, H. Liu, *et al.*, One-step self-assembly fabrication of three-dimensional copper oxide/graphene oxide aerogel composite material for supercapacitors, *Solid State Commun.*, 2019, **287**, 27–30, DOI: **10.1016/J.SSC.2018.10.007**.

62 X. Fu, Y. Sun, N. Zhou, L. Pan, M. Usman, Z. Gao, *et al.*, Facile Synthesis of A Unique Structure: CuOx@C Bead-Like Nanowire Array and Its Electrochemical Performance, *Electrochim. Acta*, 2016, **210**, 111–116, DOI: **10.1016/J.ELECTACTA.2016.05.138**.